First results from the LIFE project: discovery of two magnetic hot evolved stars

A.J. Martin, C. Neiner, M E Oksala, G A Wade, Z Keszthelyi, L Fossati, W. Marcolino, S. Mathis, C. Georgy

HAL Id: hal-01757363

https://hal.sorbonne-universite.fr/hal-01757363

Submitted on 3 Apr 2018

First results from the LIFE project: discovery of two magnetic hot evolved stars

A. J. Martin,[1]⋆ C. Neiner,[1] M. E. Oksala,[1,2] G. A. Wade,[3] Z. Keszthelyi,[3,4] L. Fossati,[5] W. Marcolino,[6] S. Mathis[1,7] and C. Georgy[8]

[1]*LESIA, Observatoire de Paris, PSL Research University, CNRS, Sorbonne Universités, UPMC Université Paris 06, Université Paris Diderot, Sorbonne Paris Cité, 5 place Jules Janssen, F-92195 Meudon, France*

[2]*Department of Physics, California Lutheran University, 60 West Olsen Road 3700, Thousand Oaks, CA, 91360, USA*

[3]*Department of Physics and Space Science, Royal Military College of Canada, PO Box 17000, Station Forces, Kingston, ON K7K 7B4, Canada*

[4]*Department of Physics, Engineering Physics and Astronomy, Queen's University, 99 University Avenue, Kingston, ON K7L 3N6, Canada*

[5]*Space Research Institute, Austrian Academy of Sciences, Schmiedlstrasse 6, A-8042 Graz, Austria*

[6]*Universidade Federal do Rio de Janeiro, Observatório do Valongo, Ladeira Pedro Antonio, 43, CEP 20.080-090, Rio de Janeiro, Brazil*

[7]*Laboratoire AIM Paris-Saclay, CEA/DRF – CNRS – Université Paris Diderot, IRFU/DAp Centre de Saclay, F-91191 Gif-sur-Yvette, France*

[8]*Geneva Observatory, University of Geneva, Chemin des Maillettes 51, CH-1290 Sauverny, Switzerland*

ABSTRACT

We present the initial results of the Large Impact of magnetic Fields on the Evolution of hot stars (LIFE) project. The focus of this project is the search for magnetic fields in evolved OBA giants and supergiants with visual magnitudes between 4 and 8, with the aim to investigate how the magnetic fields observed in upper main-sequence (MS) stars evolve from the MS until the late post-MS stages. In this paper, we present spectropolarimetric observations of 15 stars observed using the ESPaDOnS instrument of the Canada–France–Hawaii Telescope. For each star, we have determined the fundamental parameters and have used stellar evolution models to calculate their mass, age, and radius. Using the least-squared deconvolution technique, we have produced averaged line profiles for each star. From these profiles, we have measured the longitudinal magnetic field strength and have calculated the detection probability. We report the detection of magnetic fields in two stars of our sample: a weak field of $B_l = 1.0 \pm 0.2$ G is detected in the post-MS A5 star 19 Aur and a stronger field of $B_l = -230 \pm 10$ G is detected in the MS/post-MS B8/9 star HR 3042.

Key words: techniques: polarimetric – techniques: spectroscopic – stars: early-type – stars: evolution – stars: magnetic field – supergiants.

1 INTRODUCTION

The last decade has seen a remarkable increase in our knowledge of the properties of magnetic fields in main-sequence (MS) OB-type stars. As a result of a number of surveys (e.g. Fossati et al. 2015b, 2015a; Wade et al. 2016; Grunhut et al. 2017), convincing evidence indicates that ~10 per cent of MS OB stars are magnetic. This is consistent with the findings for MS A stars (Power et al. 2008; Aurière et al. 2007). MS OB stars host roughly dipolar, often oblique fossil magnetic fields (Neiner et al. 2015; Grunhut & Neiner 2015). There is currently no known mechanism to generate and sustain an efficient dynamo field in a radiative envelope, which would affect the global fossil field during the MS phase of OB-type stars (Zahn, Brun & Mathis 2007; Rüdiger, Kitchatinov & Elstner 2012; Neiner et al. 2015). The observed fossil fields likely formed in the pre-MS phases: during its formation the star could ensnare the weak field present in the interstellar medium and dynamo fields generated during pre-MS stages can enhance this seed field (Mestel 1999; Alecian et al. 2008). The field then relaxes to a stable configuration, which is mainly dipolar at the surface (Braithwaite & Spruit 2004; Duez & Mathis 2010).

Since no dynamo field is observed in MS OB stars, there is nothing to replenish the field over time. It has been shown by Bagnulo et al. (2006), Landstreet et al. (2007, 2008), and Fossati et al. (2016) that the magnetic fields at the surface of stars decrease with stellar age on the MS. This decrease in strength likely occurs in part as a result of flux conservation in response to the increase in stellar radius, possibly altered by Ohmic decay or other currently unknown effects.

Furthermore, it is likely that the stellar magnetic field has a strong influence on the evolution of the host star (Moss 1984; Langer 2012; Maeder & Meynet 2014; Keszthelyi, Wade & Petit 2017; Georgy et al. 2017). The effects of the field can be separated into

⋆ E-mail: alexander.martin@obspm.fr

those operating at the surface of the star and those in the interior. Theoretical models predict that interactions between the magnetic field and the stellar wind can reduce the surface mass loss and stellar rotation rate (ud-Doula & Owocki 2002; ud-Doula, Owocki & Townsend 2008, 2009; Meynet, Eggenberger & Maeder 2011; Bard & Townsend 2016). Indeed, studies of massive stars show that the stellar wind can become trapped in a magnetosphere rigidly coupled to the star's magnetic field (Landstreet & Borra 1978; Oksala et al. 2015). Conservation of angular momentum then leads to a decrease in the rotation rate of the star (e.g. Townsend et al. 2010; Mikulášek et al. 2007). In the stellar interior, the magnetic field has the potential to affect the mixing and diffusion of chemical elements, the internal rotational profile, and angular momentum (Mestel 1999; Mathis & Zahn 2005; Briquet et al. 2012; Sundqvist et al. 2013; Maeder & Meynet 2014; Stift & Alecian 2016).

In general, however, magnetic fields have not been taken into account in evolutionary models, except for Taylor–Spruit dynamo fields (e.g. Maeder & Meynet 2003; Heger, Woosley & Spruit 2005), which are themselves inconsistent with those observed in MS OBA-type stars. In particular, the observed fields are not correlated with rotation as would be expected for an $\alpha - \Omega$ dynamo like that proposed by Spruit (2002). It is therefore important to study these stars in detail to provide observational constraints to stellar evolution models. However, the structural changes which occur in a star during the MS are, in general, not sufficient to allow us to understand how magnetic fields change as stars evolve and how stars respond to the presence of a magnetic field.

One potential pathway towards exploring the evolution of magnetic fields in massive stars lies in the study of evolved OBA stars. We already have convincing evidence that ∼10 per cent of MS OB stars have magnetic fields (Grunhut & Neiner 2015; Fossati et al. 2015b; Grunhut et al. 2017), and the same appears to be true for PMS stars (Alecian et al. 2013). It is reasonable to suspect that the same may well be true for evolved descendants. These stars not only provide the possibility to study the evolution of magnetic fields over a longer evolutionary time frame, but also to investigate the evolution of the magnetic field in response to the significant changes in stellar structure occurring during the star's transition through the post-MS.

As the star moves through the post-MS, its radius vastly increases (e.g. Ekström et al. 2012; Georgy et al. 2013; Sanyal et al. 2015). Initially, the fossil field structure should remain unchanged, since the radiative envelope still exists and there is no mechanism to allow for the formation of a dynamo. However, as the star continues to evolve, convective zones form in the upper regions of the stellar envelope (e.g. Neiner et al. 2017). These regions have the potential to generate dynamo magnetic fields. These new dynamo fields might have a significant impact on the fossil field already present in the star (Featherstone et al. 2009; Aurière et al. 2008). Indeed the studies of FGK-type giants and supergiants show magnetic fields powered by dynamos (e.g. Grunhut et al. 2010; Aurière et al. 2015). These stars are the evolutionary descendants of OBA-type MS stars and so it is possible that a star originally with a fossil magnetic field on the MS experiences a period with both a fossil field and dynamo field, and finally evolves to a state in which only the dynamo field signature can be observed. In fact, the intermediate-mass red giant star EK Eri shows tantalizing evidence that it hosts both a dynamo field and the remnant of an Ap fossil field (Aurière et al. 2011).

Until very recently, no post-MS magnetic OBA stars had been unambiguously identified, despite high-precision studies having been conducted (e.g. Verdugo et al. 2005; Shultz et al. 2014). The O9.5 supergiant ζ Ori A was found to have a magnetic field (Bouret et al. 2008; Blazère et al. 2015), however, this star was shown to likely be still on the MS (Fossati et al. 2015a), despite its supergiant classification. A magnetic field was also detected in the B1.5 star ε CMa by Fossati et al. (2015a) and Neiner et al. (2017) showed however, that this star is also located at the end of its MS phase. As part of the BRIght Target Explorer spectropolarimetric survey (BRITEpol; Neiner et al. 2016), Neiner et al. (2017) identified two magnetic A7 supergiants: ι Car and HR 3890. Luminosity measurements and the fundamental parameters associated with these stars indicate that they are well into the post-MS phase of evolution. The detected longitudinal magnetic field strengths were found to be roughly 10 and 1 G for ι Car and HR 3890, respectively. As a result, we infer that any survey would need to be able to detect magnetic fields to a precision of better than 1 G, in order to determine the incidence rate of magnetic fields in evolved OBA-type stars.

To this end, we have started the Large Impact of magnetic Fields on the Evolution of hot stars (LIFE) project. We are observing the circularly polarized spectrum and measuring the longitudinal magnetic field strength (B_l) of OBA-type stars between $V = 4$ and 8 mag with luminosity classes I–III. In this paper, we present the analysis of the first 15 stars observed for this study. Section 2 gives details of the LIFE project, the observations, and data reduction. The fundamental parameters we infer for each star are given in Section 3 along with the evolutionary status of each star. In Section 4, we give details of the magnetic field detections and finally in Sections 5 and 6 we discuss our findings and conclude the paper.

2 THE LIFE PROJECT

Through the LIFE project, we aim to measure the distribution of magnetic field strengths in evolved stars and compare our findings with the results for MS OB stars. Any detected field will be fully characterized and the results will be compared with those of MS stars to determine how the magnetic fields of stars change as stars evolve. From this project, we aim to provide important observational constraints on theories of how magnetic fields and stellar evolution affect and interact with each other.

Choosing the appropriate exposure time for each star is critically important to give us the best possible chance of detecting magnetic fields for our sample of stars. As a result of the Magnetism in Massive Stars (MiMeS) (Wade et al. 2016), Binarity and Magnetic Interactions in various classes of stars (BinaMIcS) (Alecian et al. 2015), and BRITEpol (Neiner et al. 2016) surveys, we have an accurate exposure time relationship (Wade et al. 2016) which predicts the spectral signal-to-noise ratio (S/N) required to detect magnetic fields to a certain precision, given the spectral type and rotational velocity of a star.[1] It is then straightforward to obtain the necessary exposure time required for each star.

However, we cannot know a priori the current dipole magnetic field strength ($B_{\rm d,\,current}$) of the stars; therefore it is necessary to adopt a plausible distribution for the magnetic field. We calculate this by comparing the current radius of the star ($R_{\rm current}$) with its radius at the zero-age main sequence ($R_{\rm ZAMS}$) assuming that the magnetic flux is conserved. We calculate the expected current surface magnetic field strength to be

$$B_{\rm d,current} = B_{\rm d,ZAMS} \left(\frac{R_{\rm ZAMS}}{R_{\rm current}} \right)^2 , \qquad (1)$$

---

[1] To plan the observations, we considered the rotational velocities found through Vizier. If none were present for a given star, we assumed a value of $50 \, {\rm km \, s^{-1}}$.

where $B_{\rm d, ZAMS}$ is the magnetic field strength at the ZAMS. The choice of $B_{\rm d, ZAMS}$ is important, because we are limited by total exposure time. For this work, we assume that $B_{\rm d(ZAMS)} = 0.63\,{\rm kG}$ or if this would lead to an exposure time longer than one night, then $B_{\rm d(ZAMS)} = 1.4\,{\rm kG}$. These values correspond to 95 per cent and 85 per cent completeness of the observed distribution of magnetic field strengths in MS stars, respectively (Shultz 2016; Shultz et al. in preparation). The predicted $(\frac{R_{\rm ZAMS}}{R_{\rm current}})^2$ for our sample is between 10 and 100 which means we expect to detect dipole fields of between 7 and 140 G.

We do not, however, measure $B_{\rm d}$. Instead, we measure the mean longitudinal field $B_{\rm l}$ which is a function of the inclination angle (i) of the star and the obliquity angle (β) between the rotation axis and the magnetic axis (Preston 1967). For our stars, i and β were not available prior to the observations and so we use the equations from Preston (1967) to estimate that conservatively $B_{\rm l}$ is ~3 times weaker than $B_{\rm d}$. This lower value is factored into our calculations of the total required exposure time for each star.

2.1 Observations

The LIFE observations we present in this paper were taken using the ESPaDOnS (an Echelle SpectroPolarimetric Device for the Observation of Stars) instrument at the Canada–France–Hawaii Telescope (CFHT) and are summarized in Table 1. We observe over a wavelength range from about 3700 to 10 500 Å with a resolving power of ~68 000. Each spectrum is spread over 40 echelle orders. The observations are corrected for the bias and flat-field, and a ThAr spectrum is used to calibrate the wavelengths to the pixel values. The data were reduced using LIBRE-ESPRIT (Donati et al. 1999) and UPENA, a software pipeline available at the CFHT.

The data were taken in circular spectropolarimetric mode, measuring Stokes *I* and *V*. Each observation sequence consists of four subexposures, taken with different orientations of the Fresnel rhombs. The observations were constructively combined to form Stokes *V* and destructively combined to form the null spectra, *N* (Donati et al. 1997), using the ratio method (Bagnulo et al. 2009). Adding all four observations together provides Stokes *I*. If the total exposure time calculated in Section 2 was expected to saturate the detector, we took a number of consecutive sequences of the four subexposures which add up to the total required exposure time. These observations are then co-added after we have produced each least-squared deconvolution (LSD) profile (see Section 2.3).

2.2 Normalization of stellar spectra

We used a semi-automatic PYTHON program (Martin et al. 2017, and Appendix) to determine the continuum shape of the Stokes *I* spectrum, fitting each ESPaDOnS order individually. The PYTHON program allows the user to fit a third-order spline to the continuum. This is achieved by initially fitting a third-order spline to the reduced un-normalized spectrum. Points from the spectrum are then iteratively σ-clipped about the spline, until only continuum points remain. For the majority of spectra the σ-clipping is asymmetric with more points clipped below than above the fit (e.g. $\sigma_{\rm upper} = 3$ and $\sigma_{\rm lower} = 1$). This is because, to obtain a good continuum fit, all spectral lines must be removed and for the stars in this sample we mainly observe absorption lines. However, each parameter which determines the final continuum fit can be changed interactively including the number of iterations, the number of knots defining the cubic spline, and the σ-clipping bounds. Finally, we take the best continuum model calculated for each star and use it to normalize the Stokes *I* and *V* and *N* spectra.

Table 1. Observation log for the initial LIFE targets observed using ESPaDOnS. The name of the star, its Henry Draper catalogue (HD) designation and its Johnson *V* magnitude (Perryman et al. 1997) is given. The date of observation and the sequence of exposures is shown, where the first value is the number of consecutive polarimetric sequences, the second is the four observations taken with different rotations of the Fresnel rhombs, and the last is the number of seconds per exposure. The next column is the Heliocentric Julian Date at the middle of the observation (mid-HJD – 2450000). The average S/N of the spectropolarimetric sequence per 1.8 km s^{-1} pixel at ~5000 Å is shown, along with the mean S/N of the LSD *I* and *V* profiles computed as the mean of the square root of the diagonal elements of the inverse of the autocorrelation matrix (see Donati et al. 1997), scaled by the rms of the fit between the LSD and observed spectra. Finally, the number of lines selected for the LSD line mask following the cleaning described in Section 2.3.

Star	HD number	Visual magnitude	Date (UT)	Exposure sequence (s)	mid-HJD −2450000	Average S/N	LSD *I* S/N	LSD *V* S/N	Lines in LSD
13 Mon	46 300	4.47	2016 Feb 18	2 × 4 × 138	7437.8113	758	3536	13 603	1394
15 Sgr	167 264	5.29	2016 May 14	2 × 4 × 344	7524.1189	911	1610	6816	69
			2016 May 17	4 × 4 × 344	7526.9869	863	2229	9234	69
			2016 May 18	2 × 4 × 344	7528.0034	921	1552	6885	69
19 Aur	34 578	5.05	2016 Sep 18	5 × 4 × 254	7651.0154	1034	4031	55 620	4298
			2016 Oct 20	5 × 4 × 254	7683.0600	1067	3808	56 872	4297
24 CMa	53 138	3.02	2016 Feb 28	23 × 4 × 40	7447.8037	983	4466	48 600	538
η Leo	87 737	3.48	2016 Feb 21	5 × 4 × 50	7440.8394	535	3735	17 673	1781
γ CMa	53 244	4.11	2016 Dec 20	12 × 4 × 143	7744.0163	1111	14 049	60 259	1293
HD 10362	10 362	6.33	2016 Sep 17	1 × 4 × 991	7649.9784	1187	2270	13 094	476
			2016 Sep 19	1 × 4 × 991	7651.8850	1238	2326	13 619	476
HD 42035	42 035	6.55	2016 Sep 21	1 × 4 × 1313	7654.0594	1316	4327	22 097	2649
HD 186660	186 660	6.47	2016 Oct 13	1 × 4 × 1122	7675.7705	1112	1850	7975	327
HD 188209	188 209	5.6	2016 Jun 19	8 × 4 × 443	7560.0473	1017	1669	19 678	227
HD 209419	209 419	5.79	2016 Oct 12	1 × 4 × 666	7674.8808	1035	4305	13 777	600
HIP 38584	64 827	6.85	2017 Mar 13	1 × 4 × 1049	7826.8619	728	4861	13 323	864
HR 3042	63 655	6.23	2016 Dec 14	3 × 4 × 981	7738.0787	1233	5628	21 271	201
PT Pup	61 068	5.69	2016 Dec 20	1 × 4 × 559	7743.9491	1105	1330	13 114	304
V399 Lac	210 221	6.17	2016 Jun 14	4 × 4 × 604	7555.0612	846	2447	29 738	1631

Figure 1. The observed H β lines (black solid lines) and corresponding model spectra (red dashed line). The stars shown are those without significant wind contributions. From top to bottom the stars are: HD 186660, HD 10362, HR 3042, HD 209419, γ CMa, HIP 38584, HD 42035, and 13 Mon. Each profile is calculated with fundamental parameters as shown in Table 2.

2.3 Least-squares deconvolution

During this project, we are searching for very weak magnetic fields, between ∼1 and 100 G. This leads to Stokes V/I_c signatures with very low amplitudes. To detect such tiny signatures, we use the LSD technique (Donati et al. 1997) and combine multiple consecutive observations to increase the S/N of our data. We calculate mean LSD Stokes *I*, Stokes *V* and *N* profiles and co-add consecutive observations to produce the LSD line profiles which we use to measure the magnetic field of our observed stars. Since we aim to reduce all sources of noise we must take care when producing the line mask. The line mask is used to determine which lines to include in the LSD profile and to provide the LSD routine with the parameters of each line including their wavelength, relative depth, and Landé factor. To start, we extract a stellar line list from the Vienna Atomic Line Database3 data base (Piskunov et al. 1995; Kupka et al. 1999). This line list is calculated with the $T_{\rm eff}$ and log *g* which we determine for each of our stars (see Section 3.1). However, it will contain lines which are not present in the stellar spectrum and other lines which will add noise to the LSD profile. Therefore, we comb through each list, first removing lines with a depth smaller than 0.01 (relative to a continuum level of 1), and those which we do not see in our observed spectra. We remove hydrogen lines, because their shape is different from metal lines, and we remove any lines which blend with either H, interstellar, or strong telluric lines. Finally, we adjust the depth of each remaining line in the line mask so that it is consistent with the observed spectrum, in the manner described by Grunhut et al. (2017).

3 STELLAR PROPERTIES

3.1 Fundamental parameters

For each star, we calculated the effective temperature ($T_{\rm eff}$) and surface gravity (log *g*) using the UVBYBETA code (Napiwotzki, Schoenberner & Wenske 1993). We also used grids of synthetic spectra to visually check that the values accurately reproduce primarily the H α, H β, H γ, and H δ lines, but also regions of metal lines. Examples of the fit between the synthetic and observed spectrum for H β are shown in Fig. 1. The grids of synthetic spectra we used were calculated by Bohlin et al. (2017, using ATLAS9 model atmospheres), Martin et al. (2017, using ATLAS9 model atmospheres),

and Lanz & Hubeny (2007, using TLUSTY model atmospheres). In case of ATLAS9 model atmospheres (Kurucz 1993b), the synthetic spectra are calculated assuming plane-parallel geometry, local thermodynamic equilibrium (LTE) and opacity distribution functions for solar abundances (Kurucz 1993a). The synthetic spectra were computed with COSSAM_SIMPLE (Martin et al. 2017) and SYNTHE (Kurucz & Avrett 1981; Bohlin et al. 2017). For the TLUSTY model atmospheres, the synthetic spectra are calculated assuming non-LTE, plane-parallel geometry, and hydrostatic equilibrium using SYNSPEC (Hubeny & Lanz 2011). Where necessary we calculated additional synthetic spectra using ATLAS9 model atmospheres and SYNSPEC.

To calculate the projected rotational velocity ($v \sin i$) and the radial velocity ($v_{\rm rad}$) for each star, we first fit a Gaussian to the LSD profile. The mean value of this Gaussian is adopted as the $v_{\rm rad}$ of the star. We then subtract $v_{\rm rad}$ from the velocity of each pixel such that the line centre of the LSD profile is shifted to 0 km s^{-1}. We apply a fast Fourier transform to the profile. Following Gray (2005) and Glazunova et al. (2008), the first minimum of the transform is related to the stellar $v \sin i$ value by the limb darkening coefficient. The limb darkening value varies as a function of stellar $T_{\rm eff}$ and log *g*; for each of our stars we use limb darkening values from Claret & Bloemen (2011) which are consistent with our calculated $T_{\rm eff}$ and log *g* values.

We calculate the minimum error on $v_{\rm rad}$ ($\sigma_{v_{\rm rad}}$) following Seager, Dotson & Institute (2010) as

$$\sigma_{v_{\rm rad}} = \frac{\sqrt{{\rm FWHM}_{\rm lsd}}}{I \cdot {\rm SNR}}, \tag{2}$$

where FWHM$_{\rm lsd}$ is the full width half-maximum of the LSD profile and *I* is the maximum intensity value of the inverse of the LSD profile. We calculate the error on $v \sin i$ ($\sigma_{v \sin i}$) following Díaz et al. (2011) as

$$\sigma_{v \sin i} = 4.42 \times {\rm FWHM}_{\rm lsd}{}^{0.520} \times {\rm rms} \times I^{-1.08}, \tag{3}$$

where rms is the root mean square of the LSD profile.

To check the consistency of the calculated $v \sin i$ and $v_{\rm rad}$ values, we compare the observed spectrum with a synthetic spectrum calculated using our derived fundamental parameters and we find that they agree well.

3.2 Luminosity and evolutionary status

To determine the evolutionary status of each star, along with its radius (*R*) and mass (*M*), we use the luminosity, *L*, and the quantity $\mathcal{L} = T_{\rm eff}^4/g$. We calculate log $L/L_\odot$ using parallaxes from the *Hipparcos* data base (van Leeuwen 2007) or where available the *Gaia* data release 1 (Gaia Collaboration et al. 2016b, 2016a) and the Johnson visual magnitudes given by Perryman et al. (1997). We calculate the bolometric correction for each star following Flower (1996) and Torres (2010) using the temperatures given in Table 2. We calculate $\mathcal{L}/\mathcal{L}_\odot$ following Langer & Kudritzki (2014),

$$\log \frac{\mathcal{L}}{\mathcal{L}_\odot} = \log \left(\frac{T_{\rm eff}^4}{g} \right) - \log \left(\frac{T_{\rm eff\odot}^4}{g_\odot} \right), \tag{4}$$

where $T_{\rm eff}$ and log *g* are given in Table 2, $T_{\rm eff\odot}$ is the solar effective temperature (5756 K), and $g_\odot$ is the solar surface gravity (27542 cgs) used as calibration values for the Ekström et al. (2012) and Georgy et al. (2013) evolutionary tracks. These values are given in Table 3. For each star, we plot log $L/L_\odot$ on the theoretical Hertzsprung–Russell (HR) diagram and log $\mathcal{L}/\mathcal{L}_\odot$ on the spectroscopic HR diagram shown in the left- and right-hand panels

Table 2. Fundamental parameters of the observed stars. The name and spectral type of each star is given in the first two columns with references at the bottom of the table. The remaining columns show $T_{\rm eff}$, log g, $v \sin i$, and $v_{\rm rad}$, which were calculated according to the methods described in Section 3.1.

Star	Spectral type	$T_{\rm eff}$ (K)	log g (cgs)	$v \sin i$ (km s^{-1})	$v_{\rm rad}$ (km s^{-1})
13 Mon	A1Ib[a]	10250 ± 300	2.2 ± 0.2	13.4 ± 0.1	13.21 ± 0.02
15 Sgr	O9.7Iab[b]	30000 ± 1000	3.5 ± 0.2	58 ± 1	19.8 ± 0.1
19 Aur	A5Ib-II[c]	8500 ± 200	2.0 ± 0.2	8.8 ± 0.1	− 3.15 ± 0.01
24 CMa	B4Ia[a]	17000 ± 400	2.1 ± 0.2	39.2 ± 0.4	48.08 ± 0.07
η Leo	A0Ib[a]	9750 ± 300	2.0 ± 0.2	13.9 ± 0.1	2.82 ± 0.02
γ CMa	B6III[a]	13600 ± 300	3.4 ± 0.2	37 ± 1	31.1 ± 0.2
HD 10362	B7III[d]	14300 ± 300	3.3 ± 0.2	30.1 ± 0.7	− 6.0 ± 0.1
HD 42035	B9V[e]	10500 ± 200	3.5 ± 0.2	4 ± 1	2.3 ± 0.02
HD 186660	B2III/IV[f]	16900 ± 300	3.6 ± 0.2	11.4 ± 0.1	− 16.65 ± 0.02
HD 188209	O9.5Iab[g]	30000 ± 1000	3.1 ± 0.2	84 ± 1	− 18.78 ± 0.08
HD 209419	B5V[h]	14100 ± 300	3.5 ± 0.2	14.5 ± 0.3	− 16.23 ± 0.05
HIP 38584	B8II[i]	12600 ± 300	3.0 ± 0.2	28.4 ± 0.6	30.0 ± 0.1
HR 3042	B8/9II[j]	14150 ± 300	3.5 ± 0.2	60 ± 1	− 4.5 ± 0.2
PT Pup	B1V[k]	26300 ± 500	4.1 ± 0.2	16.9 ± 0.1	37.83 ± 0.02
V399 Lac	A3Ib[c]	8500 ± 200	1.5 ± 0.2	11.8 ± 0.1	− 25.30 ± 0.01

Notes: taken from [a]Zorec et al. (2009), [b]Sota et al. (2014), [c]Abt & Morrell (1995), [d]Jensen (1981), [e]Molnar (1972), [f]Houk & Swift (1999), [g]Sota et al. (2011), [h]Gkouvelis et al. (2016), [i]Houk (1978), [j]Houk & Smith-Moore (1988), [k]Nieva (2013).

Table 3. Stellar parameters of the observed stars. The parallax is taken from the *Hipparcos* archive (van Leeuwen 2007) or where available the *Gaia* data release 1 (denoted by *; Gaia Collaboration et al. 2016a,b). The visual magnitude is taken from the *Hipparcos* archive (Perryman et al. 1997) and the Bolometric correction is calculated following Flower (1996) and Torres (2010) using the $T_{\rm eff}$ shown in Table 2. The columns L, $\mathcal{L}$, $M_{\rm ZAMS}$, $\Omega_{\rm ZAMS}$, $R_{\rm ZAMS}$, M, R, Age, and Turn-off Age are determined as described in Section 3.2. Bold values of Age show those less than the turn-off age, therefore suggesting the star may still be on the MS. The final column shows the expected dipolar magnetic field strength for each star if the star hosted a 0.63 kG dipolar field at the ZAMS and flux conservation is the main contributing factor to the reduction of surface field strength.

Star	Parallax (mas)	$M_{\rm V}$	Bolometric correction	log L (log $L_\odot$)	log $\mathcal{L}$ (log $\mathcal{L}_\odot$)	$M_{\rm ZAMS}$ ($M_\odot$)	$\Omega_{\rm ZAMS}$ ($\Omega_{\rm crit}$)	$R_{\rm ZAMS}$ ($R_\odot$)	M ($M_\odot$)	R ($R_\odot$)	Age (Myr)	Turn-off Age (Myr)	Exp. Field (G)
13 Mon	0.8 ± 0.5	$-6.1^{+1.0}_{-1.8}$	−0.30	$4.4^{+0.4}_{-0.7}$	3.2 ± 0.1	15.0	0.60	4.7	14.7	91.9	13.8	13.6	1
						8.0	0.00	3.2	8.0	23.8	33.3	32.9	11
15 Sgr	0.1 ± 0.5	−10.0 ± 10.0	−2.89	7 ± 4	3.79 ± 0.09	32.0	0.00	6.9	30.3	18.1	**4.8**	5.2	92
						23.0	0.00	5.7	22.5	12.3	**5.9**	6.8	140
19 Aur	1.6 ± 0.3	$-4.4^{+0.4}_{-0.5}$	−0.00	3.7 ± 0.2	3.1 ± 0.1	10.0	0.00	3.6	9.7	59.3	23.8	20.9	2
						7.0	0.60	3.1	6.9	36.8	56.7	51.0	4
24 CMa	1.2 ± 0.4	$-6.7^{+0.6}_{-0.9}$	−1.53	$5.2^{+0.3}_{-0.4}$	4.2 ± 0.1	40.0	0.00	7.8	16.1	71.6	4.6	4.5	7
						15.0	0.59	4.7	14.7	29.4	13.6	13.5	16
η Leo	2.6 ± 0.2	−4.5 ± 0.1	−0.20	$3.77^{+0.05}_{-0.06}$	3.3 ± 0.2	12.0	0.98	4.8	11.9	66.6	20.3	19.2	3
						8.0	0.00	3.2	8.0	25.9	33.3	32.9	9
γ CMa	7.4 ± 0.2	−1.49 ± 0.06	−1.00	$2.88^{+0.02}_{-0.03}$	2.5 ± 0.1	7.0	0.00	2.9	7.0	11.5	42.3	41.8	41
						5.0	0.98	2.9	5.0	5.5	**98.9**	113.6	170
HD 10362	2.4 ± 0.5*	$-2.2^{+0.4}_{-0.5}$	−1.12	3.2 ± 0.2	2.7 ± 0.1	7.0	0.11	3.0	7.0	10.7	45.2	44.7	48
						5.0	0.33	2.5	5.0	5.3	**97.8**	104.5	140
HD 186660	2.1 ± 0.5*	$-2.7^{+0.5}_{-0.6}$	−1.52	3.6 ± 0.2	2.70 ± 0.09	8.0	0.00	3.2	8.0	9.4	33.2	32.9	72
						7.0	0.97	3.5	7.0	6.5	**46.5**	52.8	180
HD 188209	0.9 ± 0.2	$-5.4^{+0.5}_{-0.6}$	−2.89	5.2 ± 0.2	4.19 ± 0.09	84.9	0.00	12.2	70.0	40.9	**2.5**	3.0	56
						20.0	0.57	5.5	19.7	10.7	**7.6**	9.5	170
HD 209419	2.9 ± 0.5*	−2.1 ± 0.4	−1.09	$3.2^{+0.1}_{-0.2}$	2.5 ± 0.1	5.0	0.54	2.5	5.0	6.4	110.1	109.2	98
						5.0	0.00	2.4	5.0	5.2	**88.1**	88.2	130
HIP 38584	1.5 ± 0.4	$-2.2^{+0.5}_{-0.7}$	−0.81	$3.1^{+0.2}_{-0.3}$	2.8 ± 0.1	8.0	0.00	3.2	8.0	16.6	33.3	32.9	23
						4.0	0.58	2.2	4.0	5.1	191.0	189.4	120
HR 3042	2.8 ± 0.6*	$-1.5^{+0.4}_{-0.5}$	−1.10	2.9 ± 0.2	2.5 ± 0.1	5.0	0.54	2.5	5.0	6.3	110.1	109.2	99
						5.0	0.98	2.9	5.0	4.9	**91.7**	113.6	220
PT Pup	1.9 ± 0.3	−3.1 ± 0.3	−2.53	4.1 ± 0.1	2.96 ± 0.07	12.0	0.73	4.2	12.0	5.4	**9.1**	18.9	380
						11.0	0.00	3.8	11.0	4.5	**6.3**	17.7	450
V399 Lac	0.5 ± 0.3	$-6.7^{+1.0}_{-1.8}$	−0.00	$4.6^{+0.4}_{-0.7}$	3.6 ± 0.2	15.0	0.95	5.2	14.4	129.7	15.1	14.2	1
						7.0	0.64	3.1	6.9	38.7	58.9	51.7	4
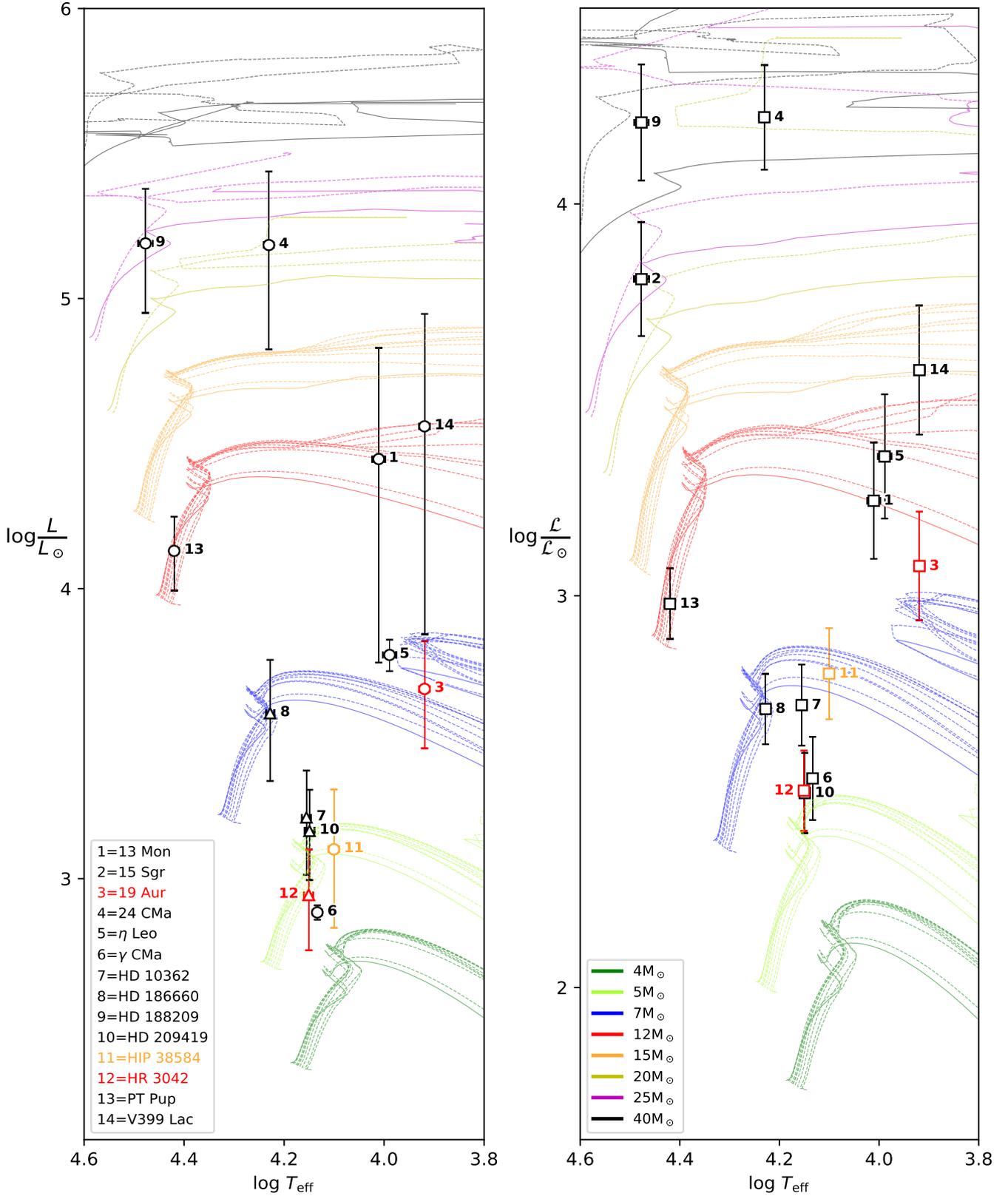
Figure 2. Left-hand panel: HR diagram of the LIFE targets, the circles are luminosities calculated with *Hipparcos* parallaxes (van Leeuwen 2007), and the triangles are with *Gaia* parallaxes (Gaia Collaboration et al. 2016a,b). Right-hand panel: spectroscopic HR diagram of the LIFE targets, where we calculate $\log(\mathcal{L}/\mathcal{L}_\odot)$ following Langer & Kudritzki (2014) shown with squares. In both panels, the evolutionary tracks from Ekström et al. (2012) and Georgy et al. (2013) are plotted (solid line, no rotation, and dashed lines with rotation from $\Omega_{ZAMS}/\Omega_{crit} = 0.1–1.0$; the colour of the isochrones denotes its mass). Red points are those stars we find to be magnetic, the orange point in each panel is the magnetic candidate, and black points are non-magnetic stars. The number closest to each point identifies the corresponding star. The error bars for $\log T_{eff}$ are plotted but, in general, they are smaller than the symbol used to indicate each star.

of Fig. 2 respectively. In addition, we plot theoretical evolutionary tracks which take into account the effects of rotation, but not the effects of magnetic fields (Ekström et al. 2012; Georgy et al. 2013).

The evolutionary tracks from Ekström et al. (2012) cover a range of ZAMS masses (M_{ZAMS}) from 0.8 to 120 $M_{\odot}$ and fractional critical velocities[2] at the ZAMS ($\Omega_{ZAMS}/\Omega_{crit}$) of 0.0 and 0.4. The models from Georgy et al. (2013) cover a range of ZAMS masses (M_{ZAMS}) from 1.7 to 15 $M_{\odot}$ and fractional critical velocities at the ZAMS ($\Omega_{ZAMS}/\Omega_{crit}$) from 0.0 to 1.0. All models used are computed with solar metallicity ($Z = 0.014$).

For each evolutionary track, a variety of stellar parameters are provided as a function of stellar age. For this study, we are particularly interested in the ratio R/R_{ZAMS} and the comparison between the age of the star, t, and the predicted age at which the star turns off the MS. To infer these values for the stars in this study, we identify the models which minimize the following expressions:

(1) $\displaystyle\operatorname*{minimize}_{M_{ZAMS},\,\Omega_{ZAMS},\,t}$

$$\left\{ \left[\frac{L_{evo}}{L_{\odot}}(M_{ZAMS}, \Omega_{ZAMS}, t) - \left(\frac{L_*}{L_{\odot}} + \sigma_{\frac{L_*}{L_{\odot}}} \right) \right]^2 + \left[T_{eff,evo}(M_{ZAMS}, \Omega_{ZAMS}, t) - \left(T_{eff,*} + \sigma_{T_{eff,*}} \right) \right]^2 \right\}^{0.5}$$

(2) Same as 1, but for $\log \mathcal{L}/\mathcal{L}\odot$

(3) $\displaystyle\operatorname*{minimize}_{M_{ZAMS},\,\Omega_{ZAMS},\,t}$

$$\left\{ \left[\frac{L_{evo}}{L_{\odot}}(M_{ZAMS}, \Omega_{ZAMS}, t) - \left(\frac{L_*}{L_{\odot}} - \sigma_{\frac{L_*}{L_{\odot}}} \right) \right]^2 + \left[T_{eff,evo}(M_{ZAMS}, \Omega_{ZAMS}, t) - \left(T_{eff,*} - \sigma_{T_{eff,*}} \right) \right]^2 \right\}^{0.5}$$

(4) Same as 3, but for $\log \mathcal{L}/\mathcal{L}\odot$.

The subscripts evo and * represent values taken from the evolutionary model and the stellar data, respectively.

In Table 3, we give the M_{ZAMS}, Ω_{ZAMS}, R_{ZAMS}, M, R, age, and turn-off age for each star, taken from two of the above models. Specifically, the first row for each star reports the parameter set described by the model 1 or 2 which maximizes M_{ZAMS}, Ω_{ZAMS}, and t. The second row reports the parameter set described by the model 3 or 4 which minimizes M_{ZAMS}, Ω_{ZAMS}, and t. The consequence of using this method is in some cases the two reported sets of values for a star may be considerably different. However, this is done in order to be conservative.

In the following subsections, we comment on our findings for each of the observed stars.

3.3 13 Mon

For 13 Mon, we determine the T_{eff} to be 10250 ± 300 K and the $\log g$ to be 2.2 ± 0.2. These values agree with those calculated by Firnstein & Przybilla (2012, T_{eff} = 10000 ± 200 K and

---

[2] The critical velocity of a star describes the stellar rotational velocity at which the centrifugal force at the equator balances with the gravitational force.
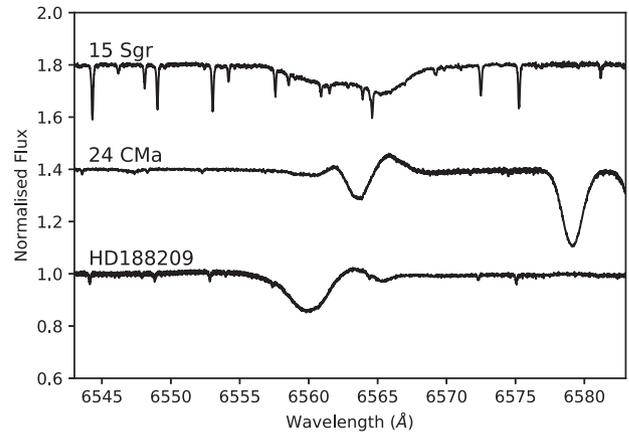
Figure 3. The observed H α lines of (from top to bottom): 15 Sgr and 24 CMa and HD 188209.

$\log g = 2.15 \pm 0.1$), but these values are slightly higher than what would be expected from a star with the spectral type of A1Ib suggested by Zorec et al. (2009). However, the plots in Fig. 2 show that 13 Mon is very clearly post-MS. We calculate an age between 13.8 and 33.3 Myr, which can be compared to the age at the MS turn-off of between 13.6 and 32.9 Myr, respectively. We conclude that it has a mass of 8–15 $M_{\odot}$ and a radius of 23.8–91.9 $R_{\odot}$. This suggests a radius increase of between a factor of 7.5 and 19.5 since the ZAMS.

3.4 15 Sgr

Analyses of 15 Sgr by Sana et al. (2014), Sota et al. (2014), and Tokovinin, Mason & Hartkopf (2010) have shown that it is a binary system. However, we do not see the presence of a companion in our spectra, likely because the magnitude of the secondary is much lower than the primary. We do see the presence of emission in H α (see Fig. 3) suggesting a stellar wind, consistent with this star being an O supergiant.

Since 15 Sgr is an O supergiant, our determination of T_{eff} and $\log g$ is focused mainly on the analysis with UVBYBETA, in addition to the results of previous studies. This is because our synthetic spectra assume a plane-parallel atmosphere. Even so, we obtain good agreement between our synthetic spectrum and the observed spectrum. The spectral type of O9.7Iab (Sota et al. 2014) and the fundamental parameters determined by Trundle et al. (2002, T_{eff} = 31500 K and $\log g$ = 3.5) and by Grunhut et al. (2017, T_{eff} = 30000 K and $\log g$ = 3.5) agree with our findings of T_{eff} (30000 ± 1000 K) and $\log g$ (3.5 ± 0.2). The uncertainty of the parallax measurement of 15 Sgr is very large, which leads to an inconclusive luminosity value. As a result, for this star, we only plot $\mathcal{L}$ in Fig. 2. Fig. 2 shows that 15 Sgr is most likely still on the MS and we calculate an age of between 4.8 and 5.9 Myr compared to the age at the MS turn-off of between 5.2 and 6.8 Myr, respectively. We conclude that it has a mass of 22.5–30.3 $M_{\odot}$ and a radius of 12.3–18.1 $R_{\odot}$. This suggests a radius increase of between a factor of 2.1 and 2.6 since the ZAMS.

3.5 19 Aur

The star 19 Aur has been studied by Lyubimkov et al. (2010) who found T_{eff} = 8300 ± 100 K and $\log g$ = 2.1 ± 0.25. This is consistent with our results of T_{eff} = 8500 ± 200 K and $\log g$ = 2.0 ± 0.2. These values also agree well with the spectral type of A5Ib-II (Abt & Morrell 1995). The plots in Fig. 2 show that 19 Aur is a post-MS star

and we calculate an age of between 23.8 and 56.7 Myr compared to the age at the MS turn-off of between 20.9 and 51.0 Myr, respectively. We conclude that it has a mass of 6.9–9.7 $M_{\odot}$ and a radius of 36.8–59.3 $R_{\odot}$. This suggests a radius increase of between a factor of 12.0 and 16.5 since the ZAMS.

3.6 24 CMa

The fundamental parameters determined by Searle et al. (2008, $T_{\rm eff} = 16500 \pm 500$ K and $\log g = 2.25$) and by Lefever, Puls & Aerts (2007, $T_{\rm eff} = 17000$ K and $\log g = 2.15$) agree with our findings of $T_{\rm eff}$ (17000 ± 400 K) and $\log g$ (2.1 ± 0.2). The parameters calculated by Fraser et al. (2010, $T_{\rm eff} = 15400$ K and $\log g = 2.15$) and by Crowther, Lennon & Walborn (2006, $T_{\rm eff} = 15500$ K and $\log g = 2.05$) are lower for both $T_{\rm eff}$ and $\log g$. However, all of the calculated parameters and the spectral type of B4Ia (Zorec et al. 2009) lead to the conclusion that 24 CMa is most likely a post-MS star or at the very end of the MS. The H α line of 24 CMa has been shown to vary in strength by 66.4 per cent (Morel et al. 2004), which could provide an explanation for the spread of results for the fundamental parameters. Our analysis is based on the inspection of a number of lines, and so should be less affected by the variation of H α. H α is in emission (see Fig. 3) which is common in Ia supergiants, but H α variation can also point to the presence of a magnetosphere and hence of a magnetic field. Therefore, this target is particularly interesting for a spectropolarimetric study.

The study by van Helden (1972) found 24 CMa to be O deficient, however Walborn (1976) found a normal CNO spectrum for a star with this spectral classification. Our findings also suggest this star has a normal CNO spectrum.

We calculate that 24 CMa has an age of between 4.6 and 13.6 Myr compared to the age at the MS turn-off of between 4.5 and 13.5 Myr, respectively. We conclude that it has a mass of 14.7–16.1 $M_{\odot}$ and a radius of 29.4–71.6 $R_{\odot}$. This suggests a radius increase of between a factor of 6.3 and 9.1 since the ZAMS.

3.7 η Leo

For η Leo, we determine the $T_{\rm eff}$ to be 9750 ± 300 K and the $\log g$ to be 2.0 ± 0.2. This agrees well with the spectral type A0Ib (Zorec et al. 2009) and with the values calculated by Firnstein & Przybilla (2012, $T_{\rm eff} = 9600 \pm 200$ K and $\log g = 2.05 \pm 0.10$). The plots in Fig. 2 show that η Leo is well into the post-MS and we calculate an age of between 20.3 and 33.3 Myr compared to the age at the MS turn-off of between 19.2 and 32.9 Myr, respectively. We conclude that it has a mass of 8.0–11.9 $M_{\odot}$ and a radius of 25.9–66.6 $R_{\odot}$. This suggests a radius increase of between a factor of 8.1 and 13.9 since the ZAMS.

3.8 γ CMa

γ CMa has been shown to be an HgMn star (Schneider 1981) and a spectroscopic binary (Schneider 1981; Schöller et al. 2010). It shows weak Y lines (Hubrig et al. 2012) and has a rotation period of 6.16 d (Briquet et al. 2010). The spectral type B6III (Zorec et al. 2009) and the fundamental parameters determined by Makaganiuk et al. (2011, $T_{\rm eff} = 13596$ K) and by Ghazaryan & Alecian (2016, $T_{\rm eff} = 13600$ K and $\log g = 3.40$) agree perfectly with our findings of $T_{\rm eff} = 13600 \pm 300$ K and $\log g = 3.4 \pm 0.2$. The plots in Fig. 2 show that γ CMa is either an MS star or at the very start of the post-MS. We calculate an age of between 42.3 and 98.9 Myr compared to the age at the MS turn-off of between 41.8 and 113.6 Myr, respectively.
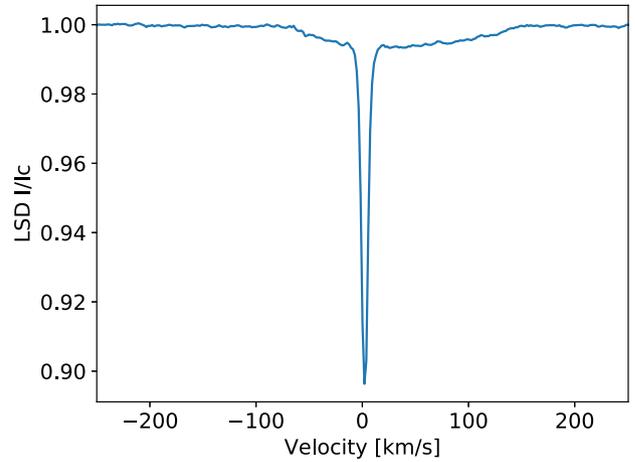
Figure 4. The LSD Stokes *I* profile of the binary star HD 42035.

We conclude that it has a mass of 5.0–7.0 $M_{\odot}$ and a radius of 5.5–11.5 $R_{\odot}$. This suggests a radius increase of between a factor of 1.9 and 3.9 since the ZAMS.

3.9 HD 10362

For HD 10362, we determine the $T_{\rm eff}$ to be 14300 ± 300 K and the $\log g$ to be 3.3 ± 0.2, which is consistent with the spectral type of B7III (Jensen 1981). The plots in Fig. 2 show that HD 10362 is post-MS or very close to the end of the MS. We calculate an age of between 45.2 and 97.8 Myr compared to the age at the MS turn-off of between 44.7 and 104.5 Myr, respectively. We conclude that it has a mass of 5.0–7.0 $M_{\odot}$ and a radius of 5.3–10.7 $R_{\odot}$. This suggests a radius increase of between a factor of 2.1 and 3.6 since the ZAMS.

3.10 HD 42035

The star HD 42035 is a binary system. Studying the LSD Stokes *I* profile of this star (Fig. 4), it can be seen that the binary consists of a very slowly rotating component and a very rapidly rotating component. This is consistent with the findings of Monier, Gebran & Royer (2016), who report numerous peculiarities of the chemical abundances, which we also observe in our spectra. We find a $T_{\rm eff}$ of 10 500 K which is consistent with the values given in Monier et al. (2016). However, as stated by Monier et al. (2016), this value has significant flux contributions from both stars, and so the evolutionary status of both stars remains unclear. For this reason, HD 42035 is not shown in Fig. 2.

3.11 HD 186660

For HD 186660, we determine the $T_{\rm eff}$ to be 16900 ± 300 K and the $\log g$ to be 3.6 ± 0.2. This suggests a star cooler than spectral type B2V (Guetter 1968), and as can be seen from Fig. 2, the $T_{\rm eff}$ and $\log g$ are consistent with the value of L given in Table 3. As a result, we conclude that HD 186660 is either at the end of the MS or at the start of the post-MS. We calculate an age of between 33.2 and 46.5 Myr compared to the age at the MS turn-off of between 32.9 and 52.8 Myr, respectively. We conclude that it has a mass of 7.0–8.0 $M_{\odot}$ and a radius of 6.5–9.4 $R_{\odot}$. This suggests a radius increase of between a factor of 1.9 and 3.0 since the ZAMS.

3.12 HD 188209

HD 188209 is an O supergiant and so, in the same way as 15 Sgr, our determination of $T_{\rm eff}$ and $\log g$ is focused mainly on the analysis of UVBYBETA and the results of previous studies. We see the presence of emission in H α (see Fig. 3), which is consistent with HD 188209 being an O supergiant. The values of $T_{\rm eff} = 31500^{+1000}_{-500}$ K and $\log g = 3.0 \pm 0.1$ found by Israelian et al. (2000) and $T_{\rm eff} = 29800 \pm 2000$ K and $\log g = 3.2 \pm 0.1$ found by Marcolino et al. (2017) agree well with our findings of $T_{\rm eff} = 30000 \pm 1000$ K and $\log g = 3.1 \pm 0.2$. These values also agree well with the spectral type of O9.5Iab. The plots in Fig. 2 show that HD 188209 is an MS star rather than on the post-MS and we calculate an age of between 2.5 and 7.6 Myr compared to the age at the MS turn-off of between 3.0 and 9.5 Myr, respectively. We conclude that it has a mass of 19.7–70.0 $M_{\odot}$ and a radius of 10.7–40.9 $R_{\odot}$. This suggests a radius increase of between a factor of 1.9 and 3.4 since the ZAMS.

3.13 HD 209419

The results by Lyubimkov et al. (2005, $T_{\rm eff} = 14100$ K and $\log g = 3.70$) are consistent with our findings of $T_{\rm eff} = 14100 \pm 300$ K and $\log g = 3.5 \pm 0.2$. These parameters suggest a star slightly cooler than the spectral type of B5V from Gkouvelis et al. (2016). The plots in Fig. 2 show that HD 209419 is either a post-MS star or at the end of the MS. We infer an age of between 110.1 and 88.1 Myr compared to the age at the MS turn-off of between 109.2 and 88.2 Myr, respectively. We conclude that it has a mass of 5.0 $M_{\odot}$ and a radius of 5.2–6.4 $R_{\odot}$. This suggests a radius increase of between a factor of 2.2 and 2.5 since the ZAMS.

3.14 HIP 38584

For HIP 38584, we determine the $T_{\rm eff}$ to be 12600 $\pm$ 300 K and the $\log g$ to be 3.0 $\pm$ 0.2, which is consistent with the spectral type of B8II (Houk 1978). The plots in Fig. 2 show that HIP 38584 is on the post-MS and we calculate an age of between 33.3 and 191.0 Myr compared to the age at the MS turn-off of between 32.9 and 189.4 Myr, respectively. We conclude that it has a mass of 4.0–8.0 $M_{\odot}$ and a radius of 5.1–16.6 $R_{\odot}$. This suggests a radius increase of between a factor of 2.3 and 5.2 since the ZAMS.

3.15 HR 3042

Our current analysis of HR 3042 suggests that this star is a He-weak chemically peculiar star. We see asymmetry in a number of spectral lines which could be caused by a binary, stellar pulsations, or indeed by the presence of a magnetic field. It is classified by Renson & Manfroid (2009) as a binary because it shows variable radial velocity. However, further analysis of spectra from multiple rotational phases is required before we can conclude about the exact nature of this star. Assuming a single star, we calculate a $T_{\rm eff}$ of 14150 $\pm$ 300 K and a $\log g$ of 3.5 $\pm$ 0.2, which is consistent with the spectral type of B8/9II (Houk & Smith-Moore 1988). The plots in Fig. 2 show that HR 3042 is most likely a post-MS star or at the end of the MS. We calculate an age of between 110.1 and 91.7 Myr compared to the age at the MS turn-off of between 109.2 and 113.6 Myr, respectively. We conclude that it has a mass of 5.0–5.0 $M_{\odot}$ and a radius of 4.9–6.3 $R_{\odot}$. This suggests a radius increase of between a factor of 1.7 and 2.5 since the ZAMS.

3.16 PT Pup

We determine $T_{\rm eff} = 26300 \pm 500$ K and $\log g = 4.1 \pm 0.2$ for PT Pup, which is consistent with the result of Nieva & Przybilla (2014, $T_{\rm eff} = 26300 \pm 300$ K and $\log g = 4.15 \pm 0.05$) and with the spectral type B1V (Nieva 2013). The plots in Fig. 2 show that PT Pup is an MS star rather than on the post-MS and we calculate an age of between 9.1 and 6.3 Myr compared to the age at the MS turn-off of between 18.9 and 17.7 Myr, respectively. We conclude that it has a mass of 11.0–12.0 $M_{\odot}$ and a radius of 4.5–5.4 $R_{\odot}$. This suggests a radius increase of between a factor of 1.2 and 1.3 since the ZAMS.

3.17 V399 Lac

The $T_{\rm eff}$ (8500 $\pm$ 200 K) and $\log g$ (1.5 $\pm$ 0.2) which we calculate for V399 Lac match well with the values calculated by Firnstein & Przybilla (2012, $T_{\rm eff} = 8400 \pm 150$ K and $\log g = 1.40 \pm 0.10$) and the spectral type A3Ib (Abt & Morrell 1995). The plots in Fig. 2 show that V399 Lac is well on to the post-MS and we calculate an age of between 15.1 and 58.9 Myr compared to the age at the MS turn-off of between 14.2 and 51.7 Myr, respectively. We conclude that it has a mass of 6.9–14.4 $M_{\odot}$ and a radius of 38.7–129.7 $R_{\odot}$. This suggests a radius increase of between a factor of 12.5 and 24.8 since the ZAMS.

4 MAGNETIC ANALYSIS AND RESULTS

The LSD profiles calculated for the LIFE targets (see Section 2.3) are shown in Figs 5–8. For each of these profiles, we calculate the longitudinal magnetic field $B_{\rm l}$ and the false alarm probability (FAP). We calculate $B_{\rm l}$ following Rees & Semel (1979) and Wade et al. (2000):

$$B_l = -2.14 \times 10^{11} \frac{\int v V(v) {\rm d}v}{\lambda z c \int [I_{\rm c} - I(v)] {\rm d}v},\tag{5}$$

where v is the position in velocity space and $I_{\rm c}$ is the Stokes I continuum level. λ and z are the wavelength in nanometres, Landé factor adopted to scale the LSD profiles, and c is the speed of light in the same unit as v. The integration limits are chosen so that they do not extend beyond the Stokes I line profile and so that they avoid the wings of the supergiants. This is because in supergiants the line wings may be formed in the stellar wind and so are not sensitive to the surface field. This is consistent with the Stokes V signatures presented by Neiner et al. (2017).

The FAP is a quantity used to determine the probability that a Stokes V signature is real or noise. It is calculated using the χ^2 probability function to ascertain whether the deviation from zero observed in the Stokes V and N profiles is best explained as a result of random noise or a signal (Donati, Semel & Rees 1992; Donati et al. 1997). We follow the convention of Donati et al. (1997), who define a definite detection to be a probability (P) that the signal is real of at least 99.999 per cent which is an FAP of 10^{-5}, a marginal detection is a 99.999 per cent > P > 99.9 per cent (10^{-5} < FAP < 10^{-3}) and no detection is P < 99.9 per cent (FAP > 10^{-3}). We require that the signal is only detected in Stokes V not in N, and that the Stokes V signal is contained within the width of the LSD Stokes I profile.

The $B_{\rm l}$ and FAP values are listed in Table 4. Comparing these results with the expected field strengths shown in Table 3, we see that we reach a magnetic precision sufficient to detect the expected field in all cases. Our results show the clear detection of a magnetic field in two of the stars: 19 Aur and HR 3042. This is also clearly
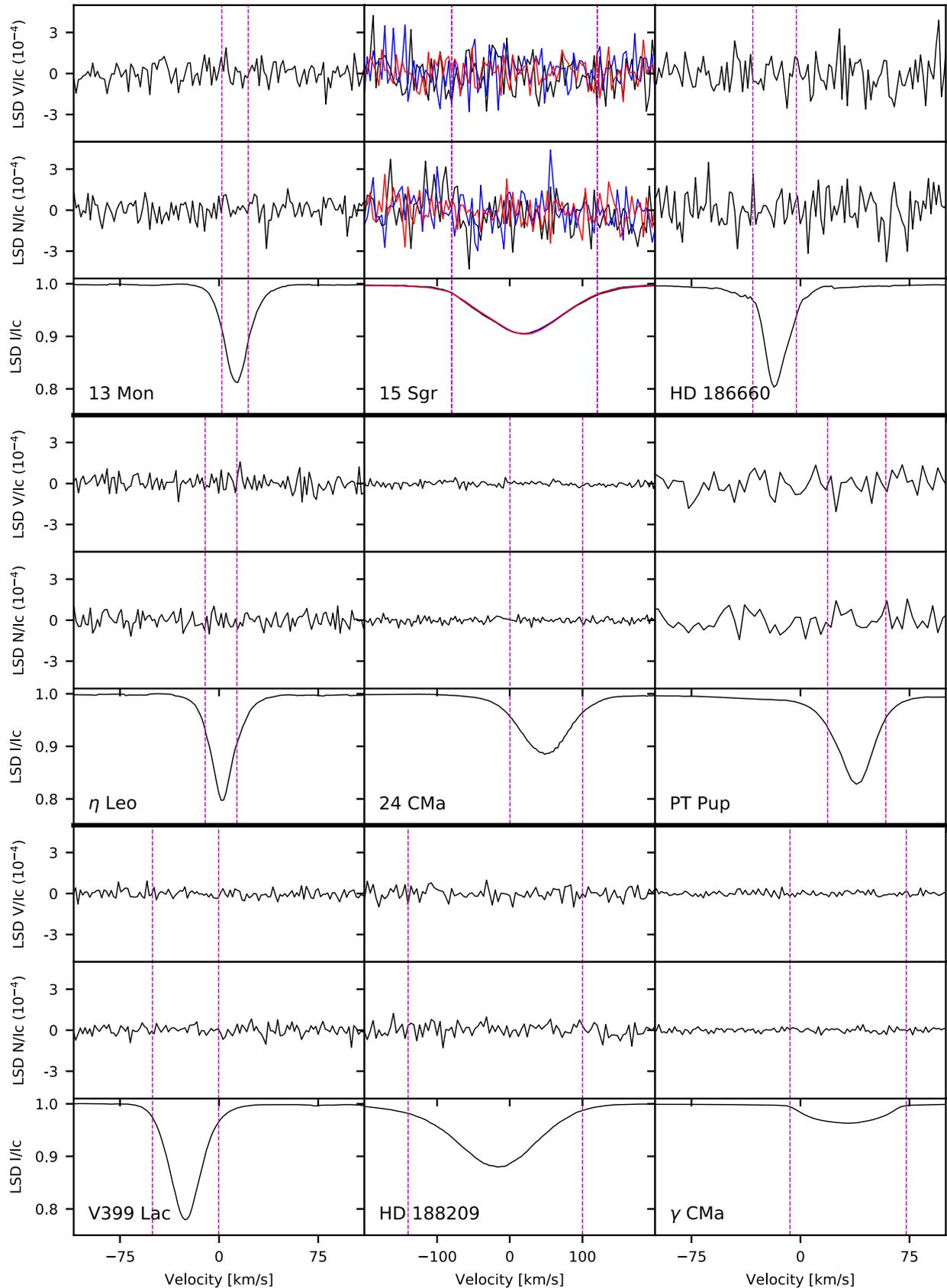
Figure 5. The LSD profiles of the LIFE targets for which no magnetic field was detected. A black solid line represents the first observation for that star in this series, blue is the second, and red is the third. The dashed lines show the integration region used to calculate the magnetic field strength and FAP.
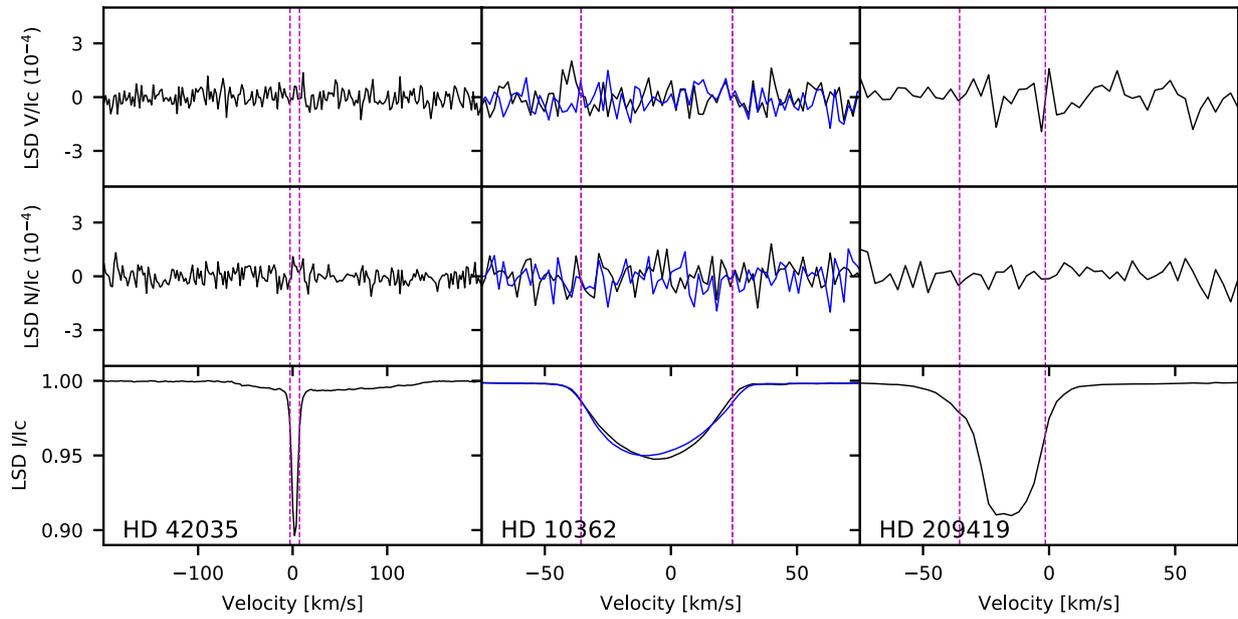
Figure 5 – *continued*
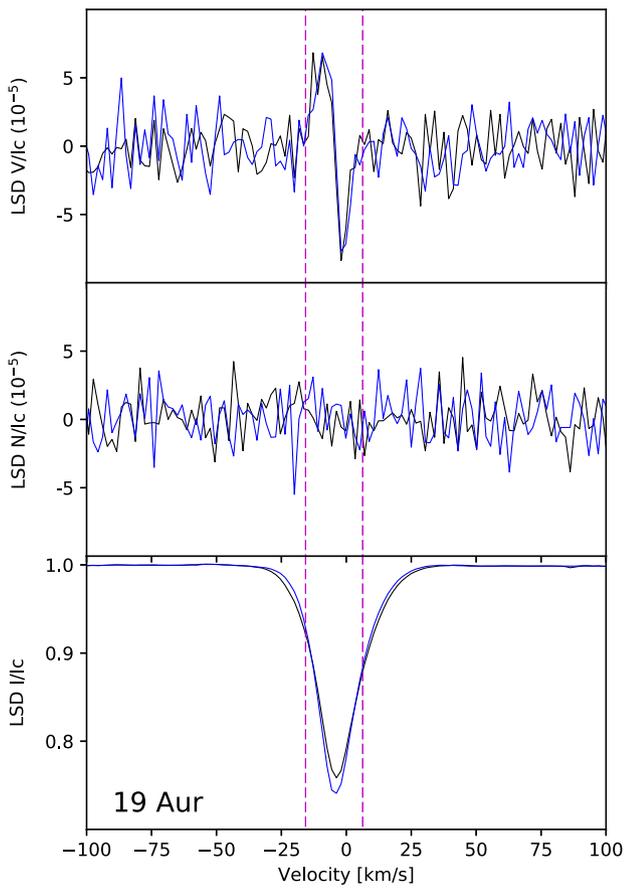
Figure 6. The LSD Stokes *I*, *N*, and Stokes *V* profiles of 19 Aur, the black line is the observation taken on the 2016 September 18 and the blue line is the observation taken on the 2016 October 20. The dashed lines show the integration region used to calculate the magnetic field strength and FAP.
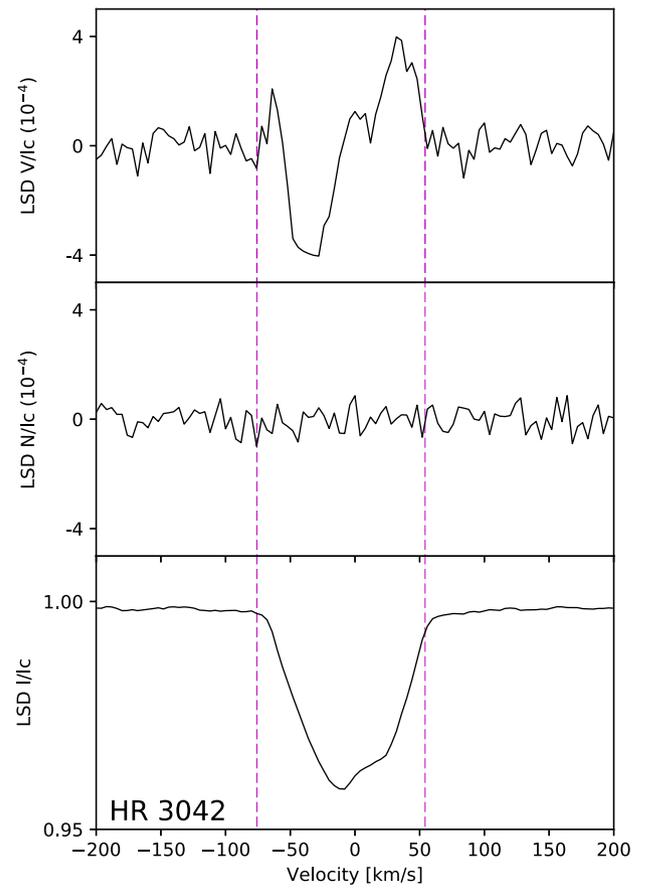
Figure 7. The LSD Stokes *I*, *N*, and Stokes *V* profiles of HR 3042, observed on the 2016 December 14. The dashed lines show the integration region used to calculate the magnetic field strength and FAP.
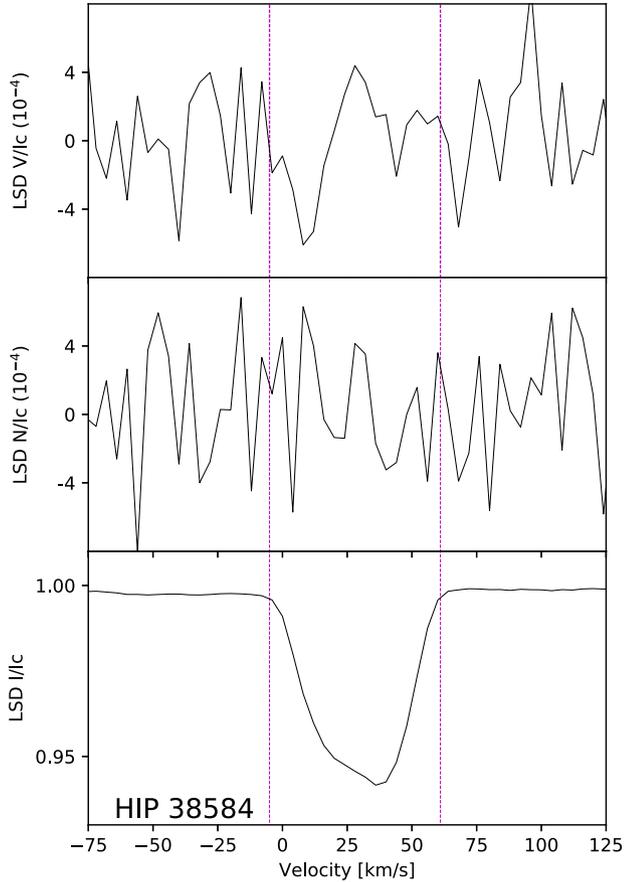
Figure 8. The LSD Stokes *I*, *N*, and Stokes *V* profiles of HIP 38584, observed on the 2017 March 13. The dashed lines show the integration region used to calculate the magnetic field strength and FAP.

Table 4. Magnetic field measurements and detection result for the observed stars. The name of the star, measured longitudinal field strength (B_l), and measured longitudinal field strength in the null profile (N_l) are given. Column 4 gives the results of the FAP analysis (see Section 4), where **DD** is a definite field detection and ND is a null detection. B_d is the current dipole field strength and B_{MS} is the estimated dipole field strength the star would have had at the ZAMS assuming only flux conservation.

Star	B_l (G)	N_l (G)	Field detect?	B_d (min) (G)	B_{ZAMS} (min) (G)
13 Mon	1.0 ± 0.6	0.5 ± 0.6	ND		
15 Sgr	0 ± 20	10 ± 20	ND		
	0 ± 20	10 ± 20	ND		
	20 ± 30	-20 ± 30	ND		
19 Aur	1.0 ± 0.2	0.3 ± 0.2	**DD**	3	470–900
	1.0 ± 0.2	-0.02 ± 0.2	**DD**	3	460–880
24 CMa	2 ± 1	0.4 ± 1.0	ND		
η Leo	0.2 ± 0.6	0.3 ± 0.6	ND		
γ CMa	9 ± 8	-4 ± 8	ND		
HD 10362	-7 ± 6	3 ± 6	ND		
	-5 ± 7	-3 ± 7	ND		
HD 42035	-0.2 ± 0.7	-0.1 ± 0.7	ND		
HD 186660	-0.8 ± 2.0	-0.4 ± 2.0	ND		
HD 188209	20 ± 20	20 ± 20	ND		
HD 209419	5 ± 3	-0.2 ± 3.0	ND		
HIP 38584	3 ± 6	7 ± 6	ND		
HR 3042	-230 ± 10	-10 ± 10	**DD**	760	2220–4810
PT Pup	-1 ± 2	1 ± 2	ND		
V399 Lac	0.9 ± 0.8	0.4 ± 0.8	ND		

observed in their LSD profiles shown in Figs 6 and 7. Moreover, HIP 38584 shows a possible Zeeman signature (see Fig. 8) which is consistent with the velocity range of the intensity line. However, its FAP leads to a non-detection and its B_l value is compatible with 0. The observations of all the other stars result in non-detections and do not show any signs of coherent structures in their Stokes *V* profiles. Below we discuss in more detail the two magnetic stars and the magnetic candidate.

4.1 The magnetic star 19 Aur

We observed 19 Aur twice, on the 2016 September 18 and October 20. Our observations consisted of five consecutive Stokes *V* sequences of four subexposures each with an exposure time of 254 s, resulting in a total exposure time of 1.41 h for each combined profile. For the line mask, 4298 lines were included after rejections based on the constraints described in Section 2.3.

We calculate B_l over an integration range of $\pm 10 \, \mathrm{km \, s^{-1}}$ about the line centre of $-3.1 \, \mathrm{km \, s^{-1}}$ for the Stokes *I* and *V* and *N* profiles. This results in a definite field detection for each observation sequence, both with a longitudinal field of $1.0 \pm 0.2 \, \mathrm{G}$ measured from the Stokes *V* profile and no detection in the *N* profile. The LSD profile of 19 Aur shows a clear antisymmetric Stokes *V* signature contained within the line centre and an essentially flat null profile, providing further evidence for a magnetic field in this star.

The two Stokes *V* profiles of 19 Aur are very similar in shape, which suggests that the rotational period is either very long (much longer than the one month that elapsed between the two observations) or by chance we observed the star in close to the same phase in both observations (suggesting a rotational period of ∼33 d or a submultiple of 33 d). A third possibility is that either *i* and/or β are close to zero resulting in a invariable Stokes *V* signature. Based on the current radius and $v \sin i$ of 19 Aur, we estimate its rotational period to be 210–340 d and thus we favour the first explanation.

We estimate $B_d > 3 \, \mathrm{G}$, which, given a current radius of between 36.8 and 59.3 $R_\odot$, suggests an estimated B_{ZAMS} of between 460 and 900 G. These values are entirely consistent with the range of magnetic field values observed in magnetic MS B stars.

4.2 The magnetic star HR 3042

We observed HR 3042 once on the 2016 December 14. Our observations consisted of three consecutive Stokes *V* sequences of four subexposures each with an exposure time of 981 s, resulting in a total exposure time of 3.27 h for the combined profile. For the line mask, 873 lines were included after rejections based on the constraints described in Section 2.3.

We calculate B_l over an integration range of $\pm 65 \, \mathrm{km \, s^{-1}}$ about the line centre of $-5 \, \mathrm{km \, s^{-1}}$ for the Stokes *I* and *V* and *N* profiles. This results in a definite field detection, with a longitudinal field of $-230 \pm 10 \, \mathrm{G}$ measured from the Stokes *V* profile and no detection in the *N* profile. The LSD profile of HR 3042 shows a very strong Stokes *V* signature and a flat null profile. This adds further evidence for a magnetic field in this star.

The Stokes *I* line profile shows an asymmetry at the core, this could be an effect of the magnetic field, stellar pulsations, binary companion, or the presence of surface spots. Further observation will allow us to determine the nature of this magnetic star.

We estimate $B_d > 760 \, \mathrm{G}$, which, given a current radius of between 4.9 and 6.3 $R_\odot$, suggests an estimated B_{ZAMS} of between 2220 and 4810 G. Thus, HR 3042 was likely a quite strongly magnetic star at

the start of the MS, and is or was possibly an Ap/Bp star. Based on the current radius and $v \sin i$ of HR 3042, we estimate its rotational period to be 4.1–5.3 d.

4.3 HIP 38584: a magnetic candidate

We have observed HIP 38584 once, on the 2017 March 13. Our observations consisted of one Stokes V sequence of four subexposures each with an exposure time of 1049 s, resulting in a total exposure time of 1.17 h for the combined profile. For the line mask, 864 lines were included after rejections based on the constraints in Section 2.3.

The FAP analysis results in no detection of a magnetic field. However, the line profile of HIP 38584 is asymmetric which could suggest a binary companion or the presence of surface spots. There is evidence of a coherent structure in half of the line profile, which could suggest that one of the two stars is magnetic. Further observations of this star are therefore necessary to determine whether or not a magnetic field is present. If this star is indeed a binary and magnetic, it will provide valuable data for the BinaMIcS (Alecian et al. 2015) project, which seeks to understand the magnetism of close binary stars.

5 DISCUSSION

Two of the stars we have observed show a clear Stokes V signature and a third shows a possible Zeeman signature in Stokes V and requires further observations to check its potential magnetic nature. Of the stars observed, six are almost certainly post-MS, five are either at the end of the MS or at the start of the post-MS and three are MS stars. The evolutionary status of HD 42035 remains unclear. This leads to an incidence rate of magnetic fields in post-MS stars of between 10 per cent and 29 per cent, which is compatible with the ∼10 per cent incidence on the MS. However, our sample of post-MS stars is so far insufficient for these values to have any statistical significance. The full LIFE sample will be necessary to draw clear conclusions.

Of the non-magnetic stars, 15 Sgr was previously studied as part of the MiMeS survey (Grunhut et al. 2017). The authors obtained only one definite field detection, which upon a visual inspection of the LSD profiles was shown to result from a coherent structure extending outside of the line profile. As a consequence, it was determined to be spurious. Our observations consist of two sets of $2 \times 4 \times 344$ s exposures and one of $4 \times 4 \times 344$ s compared with $3 \times 4 \times 300$ s (Grunhut et al. 2017). This gives us a higher overall S/N, and so the potential to detect weaker fields. Our additional observations show no evidence of a magnetic field detection or the aforementioned signature, confirming that it was almost certainly spurious. In addition, we do not detect a mean longitudinal magnetic field for γ CMa, confirming the result of Hubrig et al. (2012).

Of the two clearly magnetic stars, one is very close to or just past the turn-off point from the MS to the post-MS (HR 3042) and one is a clearly evolved star (19 Aur). HR 3042 has a current mass of $5\,M_\odot$, a T_{eff} of 14000 ± 300 K and shows an underabundance of He. Its current $B_{\mathrm{d}} > 760$ G, in combination with a predicted radius expansion of a factor between 1.8 and 2.6 suggests a magnetic field strength of at least 2220 and 4810 G at the ZAMS if magnetic flux conservation is the only process which affects the evolution of the magnetic field strength.

19 Aur has a current mass of 6.9–$9.7\,M_\odot$ and a T_{eff} of 8500 ± 200 K and we see approximately solar abundances of

elements consistent with the results of Lyubimkov et al. (2015). Its current $B_{\mathrm{d}} > 3$ G, in combination with a predicted radius expansion of a factor between 12.0 and 16.5 suggests a magnetic field strength of at least 460–900 G at the ZAMS if magnetic flux conservation is the only process which affects the evolution of the magnetic field strength. With our observations so far, we are unable to determine the type of field which exists in this star. However, since we have two observations taken 33 d apart that show essentially the same signature, there is good evidence that this star hosts only a fossil field.

The detailed magnetic and chemical abundance analyses of both HR 3042 and 19 Aur, using spectra at multiple rotational phases, will allow us to better constrain the mass, radius, metallicity, age, and field geometry for each of these stars.

Combining our findings with those of Neiner et al. (2017), there are now three known clearly evolved magnetic A-type stars: 19 Aur, ι Car, and HR 3890. The B_{ZAMS} calculated for these stars using flux conservation is consistent with distribution of magnetic field strengths on the MS for hot stars (Shultz 2016; Shultz et al. in preparation). However, these results do not exclude other possible magnetic field decay mechanisms.

6 CONCLUSIONS

In this paper, we have presented the first observations and results of the LIFE project. Out of our sample of 15 stars (six post-MS, five MS/post-MS, and three MS stars),[3] we found two to be magnetic HR 3042 and 19 Aur and a magnetic candidate, HIP 38584. HR 3042 is either at the very end of its MS lifetime or just on to the post-MS and 19 Aur is very definitely post-MS. We find that the less evolved star, HR 3042, has $B_{\mathrm{l}} = -230 \pm 10$ G and the more evolved 19 Aur has $B_{\mathrm{l}} = -1.0 \pm 0.2$ G. This is consistent with what would be expected if the field strength has decreased only as a result of flux conservation. It is important to note that the work by Fossati et al. (2016) found that magnetic flux decay likely has a significant impact on the evolution of magnetic fields. Therefore, the estimated ZAMS magnetic field strengths we calculate in this paper may be underestimated. Further analysis of the magnetic fields in evolved OBA will allow us to further understand the impact of possible magnetic flux decay.

Studying 19 Aur and HR 3042 in detail, using spectropolarimetric observations at multiple phases in each star's rotation period, will allow us to determine whether these stars still host fossil fields or whether a dynamo field has formed in the outer convective region which is modifying the fossil field. This would likely be evidenced by changes in the line profiles for the same rotation phase in different epochs. In addition, the continuation of the LIFE project is predicted to yield at least six further magnetic post-MS stars, if the prevalence of magnetic fields in these stars is consistent with their MS counterparts.

The results of the LIFE project will provide new insight on the nature of the interplay between magnetic fields and stellar evolution. The results will also provide additional evidence for theories which aim to connect the magnetic fields observed in MS stars with those observed in the later stages such as white dwarfs, neutron stars, and black holes.

---

[3] The evolutionary status of HD 42035 remains unclear because it is a binary with significant flux contributions from both stars.

ACKNOWLEDGEMENTS

REFERENCES

Abt H. A., Morrell N. I., 1995, ApJS, 99, 135
Alecian E. et al., 2008, Contribut. Astron. Obs. Skalnate Pleso, 38, 235
Alecian E. et al., 2013, MNRAS, 429, 1001
Alecian E. et al., 2015, in Meynet G., Georgy C., Groh J., Stee P., eds, Proc. IAU Symp. Vol. 307, New Windows on Massive Stars. Kluwer, Dordrecht, p. 330
Aurière M. et al., 2007, A&A, 475, 1053
Aurière M. et al., 2008, A&A, 491, 499
Aurière M., Konstantinova-Antova R., Petit P., Roudier T., 2011, in Johns-Krull C., Browning M. K., West A. A., eds, ASP Conf. Ser. Vol. 448, 16th Cambridge Workshop on Cool Stars, Stellar Systems, and the Sun. Astron. Soc. Pac., San Francisco, p. 1065
Aurière M. et al., 2015, A&A, 574, A90
Bagnulo S., Landstreet J. D., Mason E., Andretta V., Silaj J., Wade G. A., 2006, A&A, 450, 777
Bagnulo S., Landolfi M., Landstreet J. D., Landi Degl'Innocenti E., Fossati L., Sterzik M., 2009, PASP, 121, 993
Bard C., Townsend R., 2016, in Sigut T. A. A., Jones C. E., eds, ASP Conf. Ser. Vol. 506, Bright Emissaries: Be Stars as Messengers of Star-Disk Physics. Astron. Soc. Pac., San Francisco, p. 259
Blazère A., Neiner C., Tkachenko A., Bouret J.-C., Rivinius T., 2015, A&A, 582, A110
Bohlin R. C., Mészáros S., Fleming S. W., Gordon K. D., Koekemoer A. M., Kovács J., 2017, AJ, 153, 234
Bouret J.-C., Donati J.-F., Martins F., Escolano C., Marcolino W., Lanz T., Howarth I. D., 2008, MNRAS, 389, 75
Braithwaite J., Spruit H. C., 2004, Nature, 431, 819
Briquet M., Korhonen H., González J. F., Hubrig S., Hackman T., 2010, A&A, 511, A71
Briquet M. et al., 2012, MNRAS, 427, 483
Claret A., Bloemen S., 2011, A&A, 529, A75
Crowther P. A., Lennon D. J., Walborn N. R., 2006, A&A, 446, 279
Díaz C. G., González J. F., Levato H., Grosso M., 2011, A&A, 531, A143
Donati J.-F., Semel M., Rees D. E., 1992, A&A, 265, 669
Donati J.-F., Semel M., Carter B. D., Rees D. E., Collier Cameron A., 1997, MNRAS, 291, 658
Donati J.-F., Catala C., Wade G. A., Gallou G., Delaigue G., Rabou P., 1999, A&AS, 134, 149
Duez V., Mathis S., 2010, A&A, 517, A58
Ekström S. et al., 2012, A&A, 537, A146
Featherstone N. A., Browning M. K., Brun A. S., Toomre J., 2009, ApJ, 705, 1000
Firnstein M., Przybilla N., 2012, A&A, 543, A80
Flower P. J., 1996, ApJ, 469, 355
Fossati L. et al., 2015a, A&A, 574, A20
Fossati L. et al., 2015b, A&A, 582, A45
Fossati L. et al., 2016, A&A, 592, A84
Fraser M., Dufton P. L., Hunter I., Ryans R. S. I., 2010, MNRAS, 404, 1306
Gaia Collaboration et al., 2016a, A&A, 595, A1
Gaia Collaboration et al., 2016b, A&A, 595, A2
Georgy C., Ekström S., Granada A., Meynet G., Mowlavi N., Eggenberger P., Maeder A., 2013, A&A, 553, A24
Georgy C., Meynet G., Ekström S., Wade G. A., Petit V., Keszthelyi Z., Hirschi R., 2017, A&A, 599, L5
Ghazaryan S., Alecian G., 2016, MNRAS, 460, 1912
Gkouvelis L., Fabregat J., Zorec J., Steeghs D., Drew J. E., Raddi R., Wright N. J., Drake J. J., 2016, A&A, 591, A140
Glazunova L. V., Yushchenko A. V., Tsymbal V. V., Mkrtichian D. E., Lee J. J., Kang Y. W., Valyavin G. G., Lee B.-C., 2008, AJ, 136, 1736
Gray D., 2005, The Observation and Analysis of Stellar Photospheres. Cambridge Univ. Press, Cambridge
Grunhut J. H., Neiner C., 2015, in Nagendra K. N., Bagnulo S., Centeno R., Jesús Martínez González M., eds, Proc. IAU Symp. Vol. 305, Polarimetry. Kluwer, Dordrecht, p. 53
Grunhut J. H., Wade G. A., Hanes D. A., Alecian E., 2010, MNRAS, 408, 2290
Grunhut J. H. et al., 2017, MNRAS, 465, 2432
Guetter H. H., 1968, PASP, 80, 197
Heger A., Woosley S. E., Spruit H. C., 2005, ApJ, 626, 350
Houk N., 1978, Michigan Catalogue of Two-Dimensional Spectral Types for the HD Stars. University of Michigan, Ann Arbor, MI
Houk N., Smith-Moore M., 1988, Michigan Catalogue of Two-dimensional Spectral Types for the HD Stars. Vol. 4, Declinations −26 deg.0 to −12 deg.0. University of Michigan, Ann Arbor, MI
Houk N., Swift C., 1999, in Michigan Spectral Survey, Vol. 5. Department of Astronomy, University of Michigan, Ann Arbor, MI
Hubeny I., Lanz T., 2011, Astrophysics Source Code Library, record ascl:1109.022
Hubrig S. et al., 2012, A&A, 547, A90
Israelian G., Herrero A., Musaev F., Kaufer A., Galeev A., Galazutdinov G., Santolaya-Rey E., 2000, MNRAS, 316, 407
Jensen K. S., 1981, A&AS, 45, 455
Keszthelyi Z., Wade G. A., Petit V., 2017, in Eldridge J. J., Bray J. C., McClelland L. A. S., Xiao L., eds, Proc. IAU Symp. Vol. 329, The Lives and Death-Throes of Massive Stars. Kluwer, Dordrecht, p. 250
Kupka F., Piskunov N., Ryabchikova T. A., Stempels H. C., Weiss W. W., 1999, A&AS, 138, 119
Kurucz R., 1993a, Opacities for Stellar Atmospheres: [+0.0],[+0.5],[+1.0]. Kurucz CD-ROM No. 2. Smithsonian Astrophysical Observatory, Cambridge, MA
Kurucz R., 1993b, ATLAS9 Stellar Atmosphere Programs and 2 km s⁻¹ grid. Kurucz CD-ROM No. 13. Smithsonian Astrophysical Observatory, Cambridge, MA, p. 13
Kurucz R. L., Avrett E. H., 1981, SAO Special Report, 391
Landstreet J. D., Borra E. F., 1978, ApJ, 224, L5
Landstreet J. D., Bagnulo S., Andretta V., Fossati L., Mason E., Silaj J., Wade G. A., 2007, A&A, 470, 685
Landstreet J. D. et al., 2008, A&A, 481, 465
Langer N., 2012, ARA&A, 50, 107
Langer N., Kudritzki R. P., 2014, A&A, 564, A52
Lanz T., Hubeny I., 2007, ApJS, 169, 83
Lefever K., Puls J., Aerts C., 2007, A&A, 463, 1093
Lyubimkov L. S., Rostopchin S. I., Rachkovskaya T. M., Poklad D. B., Lambert D. L., 2005, MNRAS, 358, 193
Lyubimkov L. S., Lambert D. L., Rostopchin S. I., Rachkovskaya T. M., Poklad D. B., 2010, MNRAS, 402, 1369
Lyubimkov L. S., Lambert D. L., Korotin S. A., Rachkovskaya T. M., Poklad D. B., 2015, MNRAS, 446, 3447
Maeder A., Meynet G., 2003, A&A, 411, 543
Maeder A., Meynet G., 2014, ApJ, 793, 123
Makaganiuk V. et al., 2011, A&A, 525, A97
Marcolino W. L. F., Bouret J.-C., Lanz T., Maia D. S., Audard M., 2017, MNRAS, 470, 2710

Martin A. J., Stift M. J., Fossati L., Bagnulo S., Scalia C., Leone F., Smalley B., 2017, MNRAS, 466, 613

Mathis S., Zahn J.-P., 2005, A&A, 440, 653

Mestel L., 1999, Stellar Magnetism. Oxford Univ. Press, New York

Meynet G., Eggenberger P., Maeder A., 2011, A&A, 525, L11

Mikulášek Z., Krtička J., Zverko J., Žižňovský J., Janík J., 2007, in Okazaki A. T., Owocki S. P., Stefl S., eds, ASP Conf. Ser. Vol. 361, Active OB-Stars: Laboratories for Stellare and Circumstellar Physics. Astron. Soc. Pac., San Francisco, p. 466

Molnar M. R., 1972, ApJ, 175, 453

Monier R., Gebran M., Royer F., 2016, Ap&SS, 361, 139

Morel T., Marchenko S. V., Pati A. K., Kuppuswamy K., Carini M. T., Wood E., Zimmerman R., 2004, MNRAS, 351, 552

Moss D., 1984, MNRAS, 209, 607

Napiwotzki R., Schoenberner D., Wenske V., 1993, A&A, 268, 653

Neiner C., Mathis S., Alecian E., Emeriau C., Grunhut J., BinaMIcS MiMeS Collaborations 2015, in Nagendra K. N., Bagnulo S., Centeno R., Jesús Martínez González M., eds, Proc. IAU Symp. Vol. 305, Polarimetry. Kluwer, Dordrecht, p. 61

Neiner C., Wade G., Marsden S., Blazère A., 2016, preprint (arXiv:1611.03285)

Neiner C. et al., 2017, MNRAS, 471, 1926

Nieva M.-F., 2013, A&A, 550, A26

Nieva M.-F., Przybilla N., 2014, A&A, 566, A7

Oksala M. E. et al., 2015, MNRAS, 451, 2015

Perryman M. A. C. et al., 1997, A&A, 323, L49

Piskunov N. E., Kupka F., Ryabchikova T. A., Weiss W. W., Jeffery C. S., 1995, A&AS, 112, 525

Power J., Wade G. A., Aurière M., Silvester J., Hanes D., 2008, Contrib. Astron. Obs. Skalnate Pleso, 38, 443

Preston G. W., 1967, ApJ, 150, 547

Rees D. E., Semel M. D., 1979, A&A, 74, 1

Renson P., Manfroid J., 2009, A&A, 498, 961

Rüdiger G., Kitchatinov L. L., Elstner D., 2012, MNRAS, 425, 2267

Sana H. et al., 2014, ApJS, 215, 15

Sanyal D., Grassitelli L., Langer N., Bestenlehner J. M., 2015, A&A, 580, A20

Schneider H., 1981, A&AS, 44, 137

Schöller M., Correia S., Hubrig S., Ageorges N., 2010, A&A, 522, A85

Seager S., Dotson R., Institute L., 2010, Exoplanets. Space Science Series, University of Arizona Press, Arizona

Searle S. C., Prinja R. K., Massa D., Ryans R., 2008, A&A, 481, 777

Shultz M., 2016, PhD thesis, Queen's University, Kingston, Ontario, Canada

MiMeS CollaborationShultz M., Wade G. A., Petit V., Grunhut J., Neiner C., Hanes D., 2014, MNRAS, 438, 1114

Sota A., Maíz Apellániz J., Walborn N. R., Alfaro E. J., Barbá R. H., Morrell N. I., Gamen R. C., Arias J. I., 2011, ApJS, 193, 24

Sota A., Maíz Apellániz J., Morrell N. I., Barbá R. H., Walborn N. R., Gamen R. C., Arias J. I., Alfaro E. J., 2014, ApJS, 211, 10

Spruit H. C., 2002, A&A, 381, 923

Stift M. J., Alecian G., 2016, MNRAS, 457, 74

Sundqvist J. O., Petit V., Owocki S. P., Wade G. A., Puls J., MiMeS Collaboration, 2013, MNRAS, 433, 2497

Tokovinin A., Mason B. D., Hartkopf W. I., 2010, AJ, 139, 743

Torres G., 2010, AJ, 140, 1158

Townsend R. H. D., Oksala M. E., Cohen D. H., Owocki S. P., ud-Doula A., 2010, ApJ, 714, L318

Trundle C., Dufton P. L., Lennon D. J., Smartt S. J., Urbaneja M. A., 2002, A&A, 395, 519

ud-Doula A., Owocki S. P., 2002, ApJ, 576, 413

ud-Doula A., Owocki S. P., Townsend R. H. D., 2008, MNRAS, 385, 97

ud-Doula A., Owocki S. P., Townsend R. H. D., 2009, MNRAS, 392, 1022

van-Helden R., 1972, A&A, 21, 209

van-Leeuwen F., 2007, A&A, 474, 653

Verdugo E., Henrichs H. F., Talavera A., Gómez de Castro A. I., Schnerr R. S., Geers V. C., 2005, in Ignace R., Gayley K. G., eds, ASP Conf. Ser. Vol. 337, The Nature and Evolution of Disks Around Hot Stars. Astron. Soc. Pac., San Francisco, p. 324

Wade G. A., Donati J.-F., Landstreet J. D., Shorlin S. L. S., 2000, MNRAS, 313, 851

Wade G. A. et al., 2016, MNRAS, 456, 2

Walborn N. R., 1976, ApJ, 205, 419

Zahn J.-P., Brun A. S., Mathis S., 2007, A&A, 474, 145

Zorec J., Cidale L., Arias M. L., Frémat Y., Muratore M. F., Torres A. F., Martayan C., 2009, A&A, 501, 297

APPENDIX: NORMALIZATION CODE

The LIFE project involves the analysis of a large number of spectra. Part of this analysis involves fitting the continuum of each spectral order for each observation to scale the stellar continuum to unity. Generally, this is accomplished using IRAF, which is a very powerful tool. However, since we have such a large number of spectra our aim is to accomplish the normalization in a semi-automatic way. As a result, we have developed a new code, SPENT (SPEctral Normalization Tool), a PYTHON code which combines automatic σ-clipping with adjustable edge regions in an interactive interface. An example of the graphical user interface of SPENT is shown in Fig. A1.

The code begins by fitting a third-order spline to one order of an un-normalized echelle spectrum. The points which make up the spectrum are then iteratively σ-clipped until the third-order spline only passes through continuum points and so models the continuum. In this paper, we only have absorption spectra, and so we must clip more points below the fit than above, to remove the absorption lines. However, the reverse is equally possible. The user is interactively able to define the number of interior knots used to calculate the spline fit, the number of iterations of the σ-clipping and the upper and lower σ threshold values. Each time a change is made to the parameters, the normalized spectrum is updated. For each star, the normalization parameters are saved in a log file, this means it is possible to fit future observations efficiently and consistently.

A key consideration when designing this code was that the edges of the orders of echelle spectrograph can occur in the middle of spectral lines. As a result, it can be difficult to normalize these regions properly. To help overcome this issue, SPENT is built with two solutions. First, the user is able to remove a number of points at either or both ends of the un-normalized spectral order. A cluster of points at the beginning and/or end of each order replaces these. This cluster can then be move up and down which artificially adjusts the end knots of the spline. The second solution is to show a portion of the spectral orders at each side of the currently active order. This makes it possible for the user to see the characteristics of the spectral line which has been split by the orders and compensate appropriately.
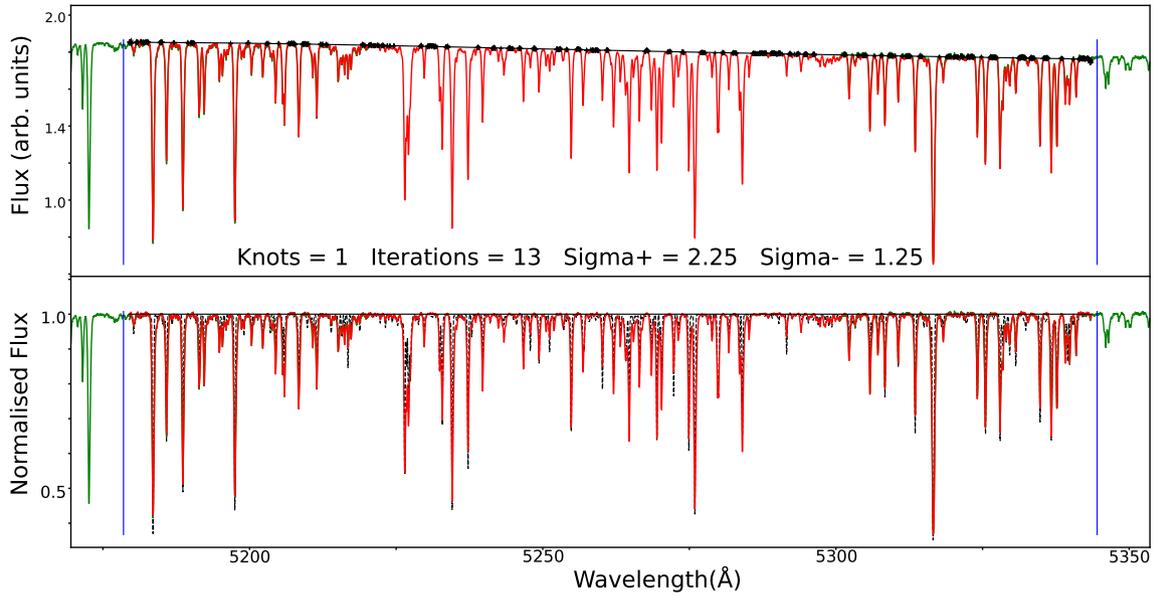
Figure A1. The graphical interface for SPENT. The upper and lower panels of the interface shows one order of the un-normalized and normalized echelle spectrum, respectively (red solid line), with a portion of the preceding and succeeding orders (green solid lines). The black pluses in the upper panel are the points calculated to be at continuum level based on the current input parameters. The solid black line is the cubic spline fit to these continuum points in the upper panel and a line at unity in the lower panel. The blue lines show the edge regions where points can be removed and replaced by a cluster of points. The current values for the input parameters are also shown and finally the dashed black line is a synthetic spectrum calculated with the fundamental parameters associated with the current star.

This paper has been typeset from a TEX/LATEX file prepared by the author.